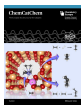

Ethene Conversion at a Zeolite-Supported Ir(I) Complex. A Computational Perspective on a Single-Site Catalyst System

Sai V. C. Vummaleti,[a] Alexander Genest,*[a, b] and Notker Rösch[b, c]

Applying a quantum mechanics/molecular mechanics scheme involving DFT calculations, a model study of mechanisms for ethene transformations at zeolite-supported Ir(I) complexes is presented and the results compared to those of recent experiments and previous work on the isostructural Rh(I) complexes. Starting from the 2-ligand complex $[Ir(C_2H_4)_2]^+$, in the presence of H_2, the ethene conversion mechanisms studied yield solely ethane while the dimerization to 1-butene *via* either the Cossee-Arlman (**CA**) mechanism or the metallacycle (**MC**) mechanism was determined to be kinetically too demanding. Therefore, turning to 3-ligand models, the calculations showed that the diethyl complex $[Ir(C_2H_4)(C_2H_5)_2]^+$ strongly favors ethene hydrogenation over dimerization (via a **CA** mechanism), with crucial activation free energies of 27 kJ mol^{-1} and 113 kJ mol^{-1}, respectively. The alternative route to dimerization via a **MC** mechanism is also not operative because the C–C coupling barrier is higher by 30 kJ mol^{-1} (in absolute terms) than the hydrogen activation in the **CA** mechanism. Thus, when Rh is substituted by Ir, the computational results allowed to rationalize the experimentally determined switching from ethene dimerization to ethane formation due to the significantly higher calculated barrier, by ~50 kJ mol^{-1} relative to Rh, of C–C coupling in the Ir system. The present study illustrates the advantage of describing the active site in a single site catalysis system, yet it also highlights the potential complexity of such systems as revealed by comparing 2- to 3-ligand models as well as models with different metal centers, Rh vs Ir, in the light of conversion rates via the energetic span concept.

Introduction

Supported metal catalysts are widely used in industrial processes.[1] Currently, single-site catalysts are intensely discussed, also for practical applications.[2] From a conceptual point of view as well as with regard to computational modeling, two classes of single-site catalysts come to mind: (*i*) single metal atoms on a metal or metal oxide support[2b,c,e] and (*ii*) mononuclear metal complexes on inorganic porous supports like zeolites, metal-organic frameworks (MOFs), and metal oxides.[2] The latter class of catalysts, of concern in the present work, are applied in alkene polymerization[3] and alkene epoxidation.[4] These catalysts are excellently suited for exploring the reaction mechanism by theory, i.e., DFT based modeling,[5] in particular when the system is experimentally well characterized.

Gates and co-workers reported[6] a well characterized zeolite-(faujasite-) supported Rh(I) complex, $[Rh(C_2H_4)_2]^+$ that exhibits a high selectivity for 1-butene (78%), with ethane as side product (19%), when the feed is ethene rich (C_2H_4/H_2 molar ratio = 4:1). The catalyst works under mild reaction conditions, 303 K and a pressure of 1 bar. In a recent DFT study, using a hybrid quantum mechanics/molecular mechanics (QM/MM) approach,[5b] we addressed the experimentally reported selectivity for ethene dimerization at a $[Rh(C_2H_4)_2]^+$ complex, probing the Cossee-Arlman mechanism[7] (**CA**) and the metallacycle mechanism[8] (**MC**), Scheme 1. Our results showed that dimerization very likely occurs from the active complex $[Rh(C_2H_4)_3]^+$, with the **MC** mechanism preferred over the **CA** mechanism. With the *in situ* generated Rh-metallacyclopentane complex acting as the active species, we were able to rationalize the experimental formation of both butene (preferred) and ethane.[5b]

Later on, Gates and co-workers extended their work to an isostructural zeolite-supported Ir(I) complex, $[Ir(C_2H_4)_2]^+$,[9] which they found to be notably less selective for ethene dimerization (11%), at 303 K and atmospheric pressure, suggesting that substituting Rh by Ir has a negative effect on the dimer formation. A recent combined experimental and computational study also reported[10] that the complex $[Ir(C_2H_4)_2]^+$, supported on the MOFs UiO-66 or NU-1000, is less selective for ethene

[a] Dr. S. V. C. Vummaleti, Dr. A. Genest
Institute of High Performance Computing
Agency for Science, Technology and Research
1 Fusionopolis Way, #16-6 Connexis
Singapore 138632 (Singapore)
[b] Dr. A. Genest, Prof. N. Rösch
Institute of Materials Chemistry
Technische Universität Wien
Getreidemarkt 9/BC
A-1060 Vienna (Austria)
E-mail: alexander.genest@tuwien.ac.at
[c] Prof. N. Rösch
Department Chemie and Catalysis Research Center
Technische Universität München
Lichtenbergstr. 4
85747 Garching (Germany)

Supporting information for this article is available on the WWW under https://doi.org/10.1002/cctc.202100615

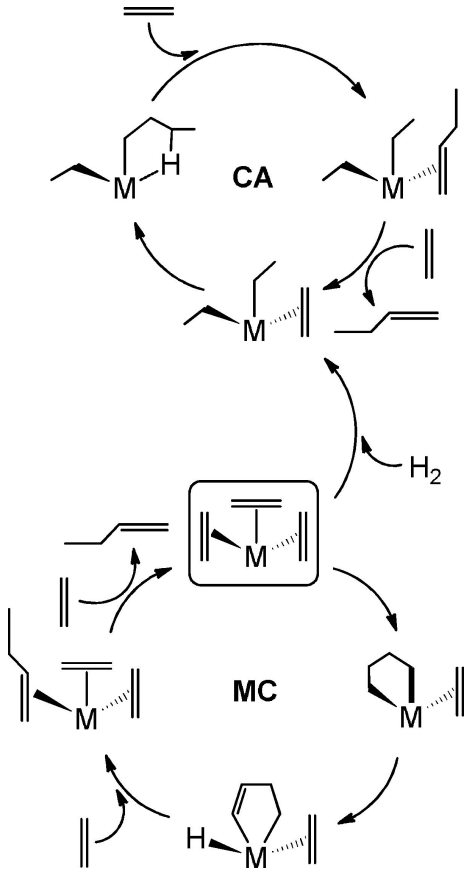

Scheme 1. Schematic representation of C–C coupling mechanisms for ethene dimerization studied here for M=Ir as metal center, using M-triethene as a reference complex. Cossee-Arlman mechanism (**CA**, top): ethene insertion into a metal-ethyl bond; metallacycle mechanism (**MC**, bottom): direct coupling of two ethene moieties forming a metallacyclopentane.

dimerization (< 5 %). Until now, there exist only few theoretical studies for the important supported catalytic system $[Ir(C_2H_4)_2]^+$, addressing structural features of the supported complexes[11] and some steps of ethene conversion, i.e., hydrogenation and dimerization.[10,12] Yet, none of these studies offered a detailed *mechanistic* comparison of both types of processes.

In the present computational work, we explore mechanistic details of the ethene conversion for a zeolite-supported Ir(I) complex **1**, $[Ir(C_2H_4)_2]^+$, Scheme 2, using DFT calculations with the QM/MM approach[5b] previously applied to analogous Rh complexes. Based on these earlier findings,[5b] we also explored the mechanism when starting from the alternative complex **14**, $[Ir(C_2H_4)_3]^+$, Schemes 3, 4, and 5. These ethene conversion mechanisms, using starting complexes **1** or **14**, with two or three organic ligands at the Ir metal center (ethene or ethyl), will be addressed as 2-ligand models and 3-ligand models, respectively.[5]

Finally, we will compare the computational results from these Ir(I) complexes for the crucial hydrogenation and C–C coupling steps to the previously reported results for Rh(I) complexes,[5] to gain insight into how the choice of the metal M (M = Ir or Rh) might affect the product selectivity, ethane *vs*

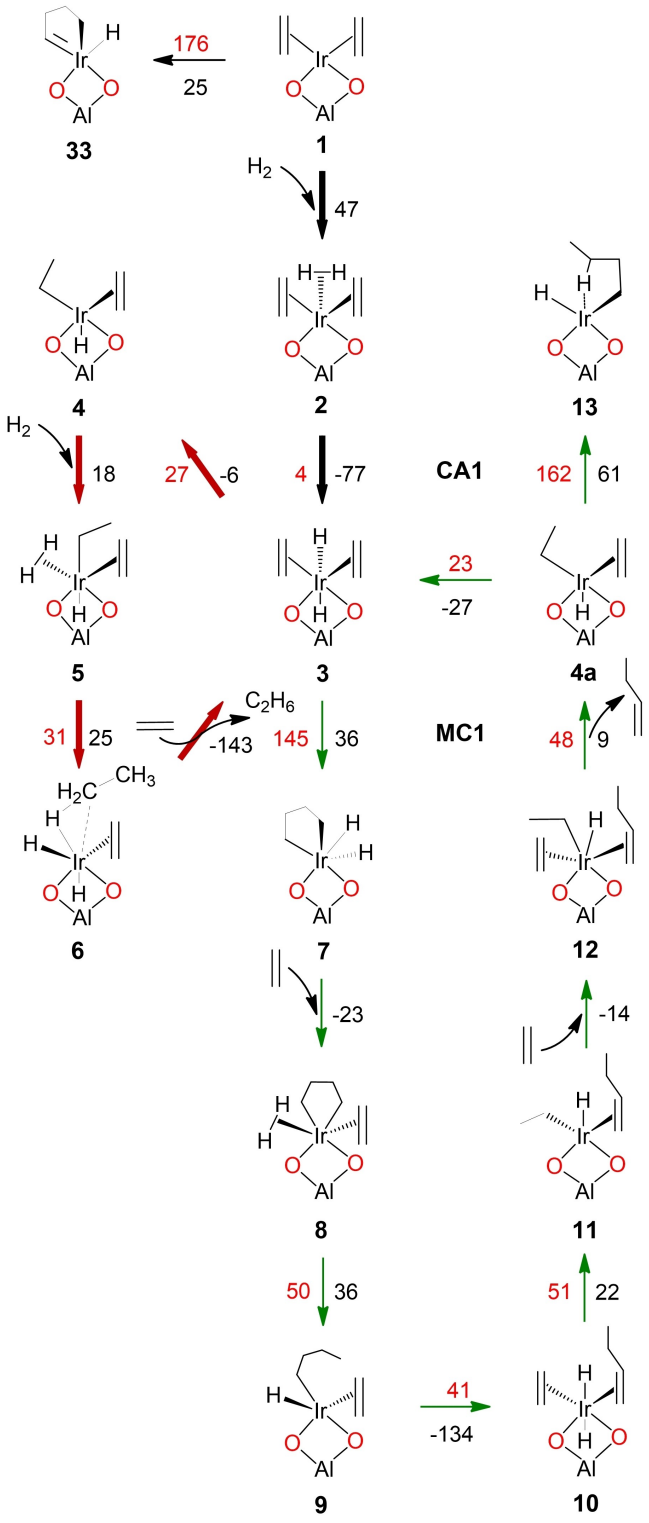

Scheme 2. Reaction network of ethene hydrogenation and dimerization via the Cossee-Arlman mechanism, pathway **MC1** for the zeolite-supported 2-ligand Ir(I) complex **1**, $[Ir(C_2H_4)_2]^+$. Reaction and activation free energies of individual steps are given as black and red values, in kJ mol^{-1}. Bold arrows indicate the most favorable pathway. Black arrows mark the common steps leading to complex **3**, the branching point for the pathways to ethane and 1-butene. Red arrows mark reaction steps leading to ethane formation. Green arrows label conversions towards ethene dimerization. For simplicity, the zeolite support of the metal complex is represented by the O–Al–O moiety.

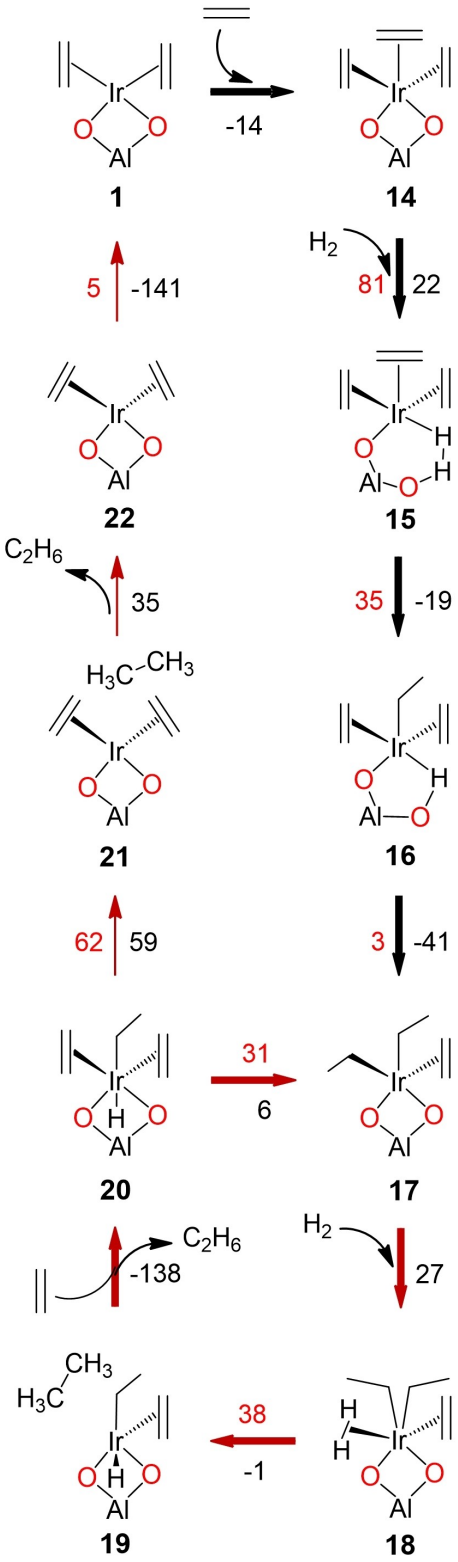

Scheme 3. Reaction network of ethene hydrogenation using a 3-ligand model. Lay-out as in Scheme 2. The side reaction, starting at branching point **20** yields a second ethane moiety.

butene, and the preferential ethene dimerization mechanism, **CA** *vs* **MC**. Given this modeling experience, we will also briefly comment on the challenges posed by the two classes of single-site catalysts mentioned above.

Results and Discussion

2-ligand models

We start by briefly discussing the mechanisms of ethene conversion from complex **1**, $[Ir(C_2H_4)_2]^+$, Scheme 2. Next, we will compare the crucial free energy barriers of hydrogenation and C–C coupling steps to the previously elaborated results, obtained with the same QM/MM strategy for the isostructural zeolite-supported complex $[Rh(C_2H_4)_2]^+$.[5b]

Ethene conversion mechanism for complex 1, $[Ir(C_2H_4)_2]^+$. Scheme 2 presents the pathways of ethene hydrogenation and dimerization studied, starting from complex **1**, $[Ir(C_2H_4)_2]^+$; see also the corresponding energy profile in Figure 1. Note that for all the schemes presented in this study, we provide relative free energy barriers of each step, together with the corresponding reaction free energies. Figure S2 of the Supporting Information shows a complete energy profile including alternative, less favorable pathways.

Ethene hydrogenation. The coordination of H_2 to the Ir center of complex **1**, an endergonic step, G_r(**1**→**2**) = 47 kJ mol^{-1}, leads to complex **2**, $[Ir(C_2H_4)_2(H_2)]^+$, Scheme 2 and Figure 1. The oxidative addition of H_2 at the Ir center of **2** is highly exergonic, G_r(**2**→**3**) = −77 kJ mol^{-1}, forming complex **3**. This rate-determining step requires overcoming an overall free energy barrier of G_a(**1**→**2**→**3**) = 51 kJ mol^{-1}, Scheme 2 and Figure 1, that is lower by only 3 kJ mol^{-1} than in the analogous step for the complex $[Rh(C_2H_4)_2]^+$, 54 kJ mol^{-1}.[5b] Note that Complex **3** acts as a branching point on the way to ethene hydrogenation or dimerization via the metallacycle mechanism, pathway **MC1**, Scheme 2 and Figure 1.

Hydrogenation of the ethene ligand in **3** yields the slightly more stable complex **4**, $[Ir(C_2H_4)(C_2H_5)(H)]^+$, G_r(**3**→**4**) = −6 kJ mol^{-1}, via a moderate barrier, G_a(**3**→**4**) = 27 kJ mol^{-1}. Next, coordination of a further H_2 molecule to the Ir center of **4** produces complex **5**, $[Ir(C_2H_4)(C_2H_5)(H)(H_2)]^+$, with an endergonic free energy change G_r(**4**→**5**) = 18 kJ mol^{-1}, Scheme 2 and Figure 1. Hydrogenation of the ethyl ligand in **5** yields the desired ethane complex **6**, $[Ir(C_2H_4)(H_2)(C_2H_6)]^+$, G_r(**5**→**6**) = 25 kJ mol^{-1}, featuring a moderate overall free energy barrier, G_a(**4**→**5**→**6**) = 49 kJ mol^{-1}, Scheme 2 and Figure 1. Finally, complex **6** releases the product ethane into the gas phase, closing the catalytic cycle at **3** by coordinating a further free ethene ligand, G_r(**6**→**3**) = −143 kJ mol^{-1}, Scheme 2 and Figure 1. Note that the ethene uptake involves first a transfer into the zeolite cavity, a state that is by less than 5 kJ mol^{-1} higher in free energy. When releasing ethane or butene, these two steps are reversed in order. Overall, for hydrocarbons (ethene, ethane, and butene) we determined minor changes in free energy when transferring them into the zeolite cavity, about ±5 kJ mol^{-1}, which we will not account for when discussing variants of mechanisms.

Thus, different from the analogous process at the Rh complex, the ethene hydrogenation at the Ir complex avoids

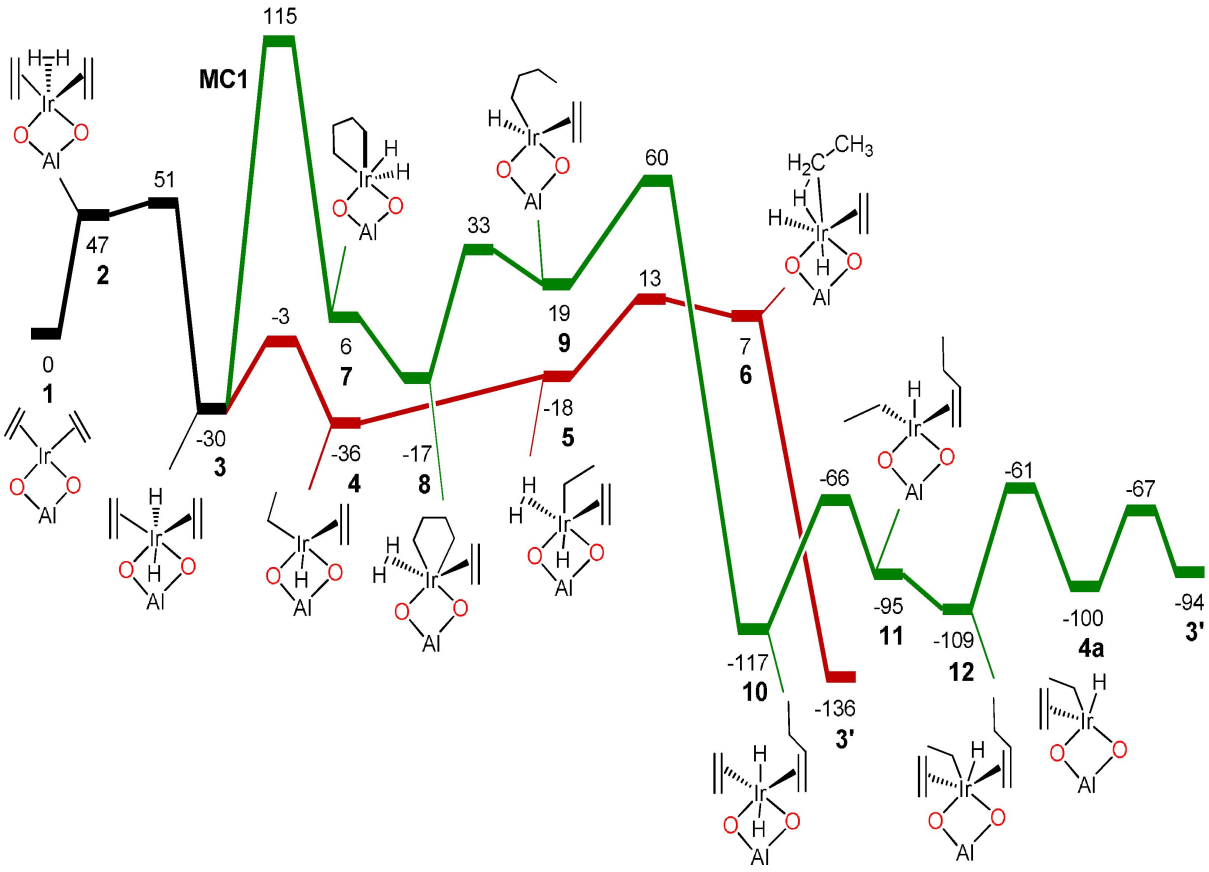

Figure 1. Slightly simplified free energy profile for the hydrogenation and the dimerization of ethene via the metallacycle mechanism **MC1** starting from the zeolite-supported 2-ligand Ir(I) model complex **1**, $[Ir(C_2H_4)_2]^+$. Free energies (kJ mol^{-1}) with respect to complex **1** as well as H_2 and C_2H_4 in the gas phase, at formally infinite separation. Only the lowest-lying pathways are shown; for variants, see Figure S2 of the Supporting Information. Intermediates are labeled and shown in sketches; a prime to the label for species produced a second time along the reaction pathway. Color coding: red – product ethane; green – product butene; black – joint section of the pathway.

cycling through the oxidative addition of H_2 over the free energy barrier via TS **2**→**3**, 51 kJ mol^{-1} above **1**, by restarting the catalytic cycle directly from **3**. In consequence, this pathway beginning at complex **1** utilizes two molecules of H_2 only once, in the first catalytic cycle. As the initial complex **3** is at −30 kJ mol^{-1}, one determines a free energy change of −106 kJ mol^{-1} for converting one molecule of ethene and H_2 to ethane, Scheme 2 and Figure 1. This result agrees remarkably well with the corresponding experimental free energy change of −101 kJ mol^{-1} at 298 K and 1 bar.[13] Note that for the studied 2-ligand Ir models, we determined oxidation state +3 as prevalent over oxidation state +1, Scheme 2 and Figure 1, analogous to the case of Rh.[5b] Overall, 2-ligand Ir models have two complexes with oxidation state +1, **1** and **2**, while the remaining 10 complexes feature oxidation state +3, Scheme 2 and Figure 1. The dominance of Ir(III) chemistry is evident as it occurs at the crucial branching points, **3** and **4**, as well as at the most stable species **10** of the 2-ligand based ethene conversion mechanism, Scheme 2 and Figure 1.

Selective C–C coupling via a metallacycle mechanism (MC). Complex **3** is also on the C–C coupling path **MC1**. Note that the oxidative coupling of two ethene ligands in complex **1** did not result in a stable metallacyclopentane species. Rather, one of the α-H moieties is transferred to the metal center, forming the metallacyclopentenyl complex **33**, G_r(**1**→**33**) = 25 kJ mol^{-1}, Scheme 2. This step requires overcoming an extremely high barrier, G_a(**1**→**33**) = 176 kJ mol^{-1}, which may be due to the relatively low coordination number of the metal center when its oxidation state changes from +1 to +3. Complex **33**, a square pyramidal structure, is coordinatively unsaturated and does not lead to any of the products under discussion, butene or ethane. Thus, we refrained from discussing complex **33** any further. In the light of recent DFT studies,[5b,10] we here explored C–C coupling reaction at complex **3**, leading to the formation of metallacyclopentane complex **7**, G_r(**3**→**7**) = 36 kJ mol^{-1}, Scheme 2 and Figure 1. The C–C coupling step **3**→**7** with the activation free energy, G_a(**3**→**7**) = 145 kJ mol^{-1} (115 kJ mol^{-1} above **1**) is the first step on pathway **MC1**, Scheme 2 and Figure 1.

Coordination of an ethene species at the Ir center of **7** leads to **8**, G_r(**7**→**8**) = −23 kJ mol^{-1}, Scheme 2 and Figure 1. In the next step, the metallacycle ring of complex **8** opens, cleaving an Ir–CH_2 bond by hydrogenating that terminal –CH_2 group, to yield the butyl complex **9**, $[Ir(C_2H_4)(H)(C_4H_9)]^+$. This step is

endergonic, G_r(**8**→**9**) = 36 kJ mol^{-1}, over a moderate free energy barrier, G_a(**8**→**9**) = 50 kJ mol^{-1}, Scheme 2 and Figure 1. Rotation of the butyl ligand in **9** around the C1–C2 bond, followed by the transfer of β-hydrogen to the Ir center in a concerted fashion produces the desired butene complex **10**, [Ir-(C_2H_4)(H_2)(C_4H_8)]$^+$. This latter step is highly exergonic, G_r(**9**→**10**) = −134 kJ mol^{-1}, and occurs via a moderate free energy barrier, G_a(**9**→**10**) = 41 kJ mol^{-1}, Scheme 2 and Figure 1. Complex **10** regenerates complex **3** by removing butene via **10**→**11**→**12**→**4a**, and transferring a H atom from the ethyl moiety in **4a** to the metal center, forming complex **3**, Scheme 2 and Figure 1.

Hydrogenation of the ethene ligand in **10** generates the Ir-ethyl complex **11**, [Ir(C_2H_5)(H)(C_4H_8)]$^+$, G_r(**10**→**11**) = 22 kJ mol^{-1}, via a moderate free energy barrier, G_a(**10**→**11**) = 51 kJ mol^{-1}, Scheme 2 and Figure 1. Coordination of a further ethene molecule to the Ir center of **11** is slightly exergonic and yields complex **12**, [Ir(C_2H_4)(C_2H_5)(H)(C_4H_8)]$^+$, G_r(**11**→**12**) = −14 kJ mol^{-1}, Scheme 2 and Figure 1. Next, butene is released into the gas phase from complex **12** in a slightly endergonic step, G_r(**12**→**4a**) = 9 kJ mol^{-1}, leading back to complex **4**, over a moderate activation free energy barrier, G_a(**12**→**4a**) = 48 kJ mol^{-1}, Scheme 2 and Figure 1. Finally, complex **4a** regenerates complex **3** by transferring a H atom from the ethyl moiety to the metal center, G_r(**4a**→**3′**) = 6 kJ mol^{-1}, thus starting a new catalytic cycle, Scheme 2 and Figure 1. This step entails a moderate barrier, G_a(**4a**→**3′**) = 33 kJ mol^{-1}, Scheme 2 and Figure 1. From the catalytic cycle, Scheme 2, one determines a free energy change of −64 kJ mol^{-1} for forming butene from two molecules of ethene, Figure 1. This result agrees remarkably well with the corresponding experimental free energy change, −66 kJ mol^{-1} at 298 K and 1 bar.[13]

Alternatively, the C–C coupling between two ligands of **4**, ethene and ethyl, Scheme 2 via the Cossee-Arlman mechanism, pathway **CA1**, yields the butyl complex **13**, [Ir(H)(C_4H_9)]$^+$. This step requires overcoming an extremely high activation barrier, G_a(**4**→**13**) = 162 kJ mol^{-1}, Scheme 2, that is by 17 kJ mol^{-1} higher than the competing barrier via pathway **MC1**, G_a(**3**→**7**) = 145 kJ mol^{-1}, favoring the latter transformation, Scheme 2 and Figure 1.

In summary, the mechanism examined for complex **1** suggests that the barrier to ethane formation via TS **5**→**6**, 13 kJ mol^{-1} above **1**, is lower by 102 kJ mol^{-1} than the C–C coupling barrier of butene formation via TS **3**→**7**, 115 kJ mol^{-1} above **1**, suggesting the preference for forming ethane as the major product, Scheme 2 and Figure 1. Less likely pathways, namely the formation of ethane (**5**→**28**→**29**→**4′**) as well as a path leading to both ethane and butene (**12**→**30**→**26**→**1′**), are further discussed in Section S2 of the Supporting Information.

3-ligand models

Motivated by our previous work[5b] where we addressed ethene transformations over a zeolite-based Rh complex with *three* ethene ligands, we will examine in the following pathways to ethene hydrogenation and dimerization starting from complex **14**, [Ir(C_2H_4)$_3$]$^+$. That complex may be formed by the slightly exergonic ethene association at the di-ethene complex **1**, Scheme 3 and Figure 2. First, we will present the transformations leading from the structure **14** to the branching point **17**, [Ir(C_2H_5)$_2$(C_2H_4)]$^+$. As in our discussion of 2-ligand models, we briefly discuss ethene hydrogenation, followed by presenting the dimerization of ethene *via* metallacycle mechanisms, pathways **MC2** and **MC3**; see Schemes 3, 4 and Figures 2, 3. We shall conclude this section with an ethene dimerization variant according to a Cossee-Arlman-type mechanism, pathway **CA2**, Scheme 5 and Figure 2.

Formation of the branching complex 17. The coordination of ethene to the Ir center of complex **1** is slightly exergonic, G_r(**1**→**14**) = −14 kJ mol^{-1}, forming the three-ethene complex **14**, [Ir(C_2H_4)$_3$]$^+$, Scheme 3. Complex **14** is thermodynamically preferred by 61 kJ mol^{-1} compared to the dihydrogen complex **2**, Schemes 2 and 3. In the following, we will use complex **14** as reference of absolute (free) energies. Figures 2 and 3 provide simplified energy profiles of the catalytic cycles for ethene hydrogenation and dimerization via the 3-ligand model path.

Similar to the analogous process at the 3-ligand Rh(I) complex,[5b] we probed the activation of H_2 by inserting it into the Ir–O1 bond of **14**, forming complex **15** with the bridge Ir–H1–H2–O1; Ir–H1 = 163 pm, H1–H2 = 192 pm, O1–H2 = 103 pm, Scheme 3 and Figure S8 of the Supporting Information. This step is somewhat endergonic, G_r(**14**→**15**) = 22 kJ mol^{-1}, requiring to overcome a notable free energy barrier, G_a(**14**→**15**) = 81 kJ mol^{-1}, Scheme 3 and Figure 2. The subsequent hydrogenation of the ethene ligands of complexes **15** passing structure **16** yields the crucial diethyl complex **17**, [Ir-(C_2H_5)$_2$(C_2H_4)]$^+$ that acts as a branching point between both reaction types, ethene dimerization and hydrogenation, Schemes 3, 5, and Figure 2. The formation of **16** is exergonic, G_r(**15**→**16**) = −19 kJ mol^{-1}, over a moderate barrier, G_a(**15**→**16**) = 35 kJ mol^{-1}, while the moderately exergonic formation of the crucial complex **17**, G_a(**16**→**17**) = −41 kJ mol^{-1}, occurs essentially without a barrier, G_a(**16**→**17**) = 3 kJ mol^{-1}.

Ethene hydrogenation starting from complex 17. Complex **17** is part of the path of ethene hydrogenation along the catalytic cycle **17**→**18**→**19**→**20**→**17′**, Scheme 3 and Figure 2. Coordination of H_2 to **17** is calculated endergonic, G_r(**17**→**18**) = 27 kJ mol^{-1}, forming complex **18**, [Ir(C_2H_5)$_2$(C_2H_4)(H_2)]$^+$. Next, the hydrogenation of one of the ethyl ligands in **18** yields the ethane coordinated complex **19**, [Ir(C_2H_5)(H)(C_2H_4)(C_2H_6)]$^+$, Scheme 3. This step is thermoneutral, G_r(**18**→**19**) = −1 kJ mol^{-1}, over a moderate barrier, G_a(**18**→**19**) = 38 kJ mol^{-1}, Scheme 3 and Figure 2.

Complex **19** regenerates complex **17** (as **17′**) in two steps. Releasing the product ethane into the gas phase by coordinating a free ethene ligand leads to complex **20** in a highly exergonic fashion, G_r(**19**→**20**) = −138 kJ mol^{-1}, Scheme 3 and Figure 2. Hydrogenation of one of the ethene ligands of complex **20** regenerates the active species **17** (as **17′**), thus closing the catalytic cycle, Scheme 3 and Figure 2. This final step is slightly endergonic, G_r(**20**→**17′**) = 6 kJ mol^{-1}, requiring to overcome a moderate activation barrier, G_a(**20**→**17′**) = 31 kJ mol^{-1}.

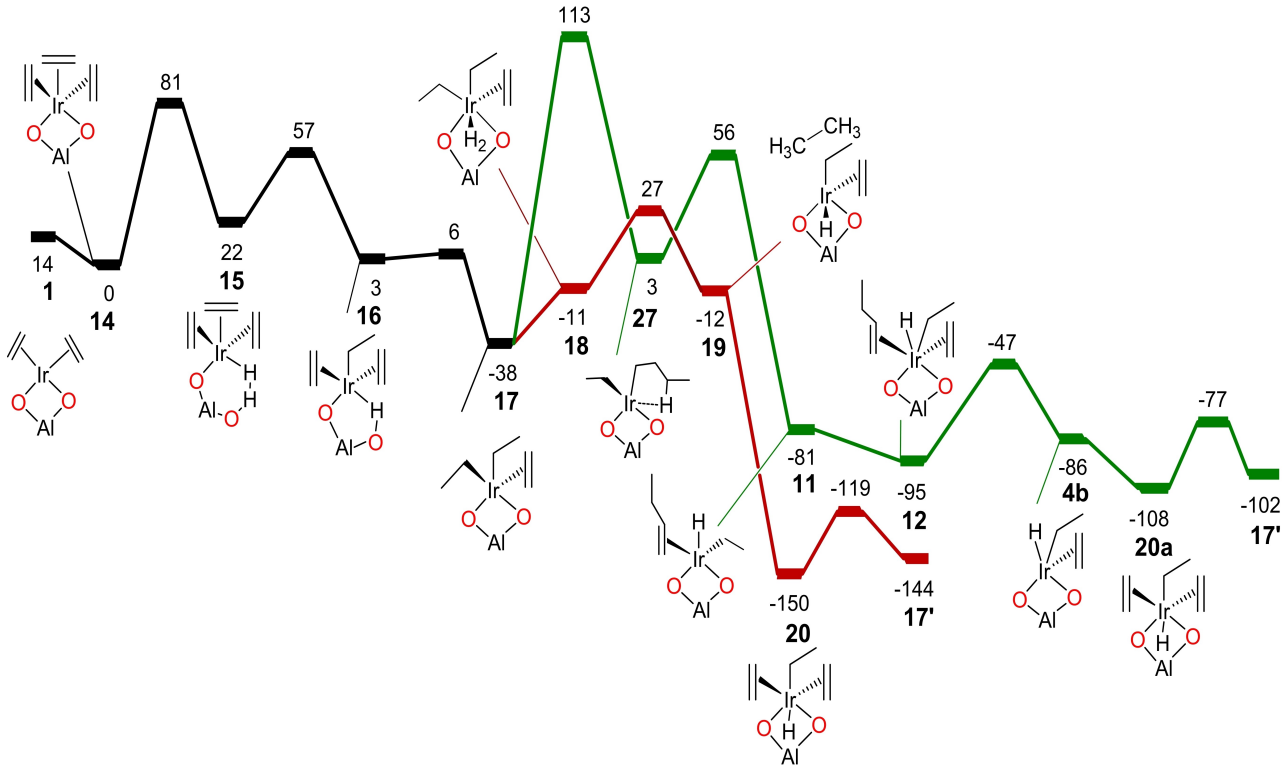

Figure 2. Simplified free energy profile for ethene hydrogenation and dimerization via the pathway **CA2** starting from the 3-ligand Ir(I) complex **14**, $[Ir(C_2H_4)_3]^+$. Free energies (kJ mol^{-1}) with respect to complex **14** as well as H_2 and C_2H_4 in the gas phase, at infinite separation. Only the lowest-lying pathways are shown; for variants, see Figure S3 of the Supporting Information. Lay-out as in Figure 1.

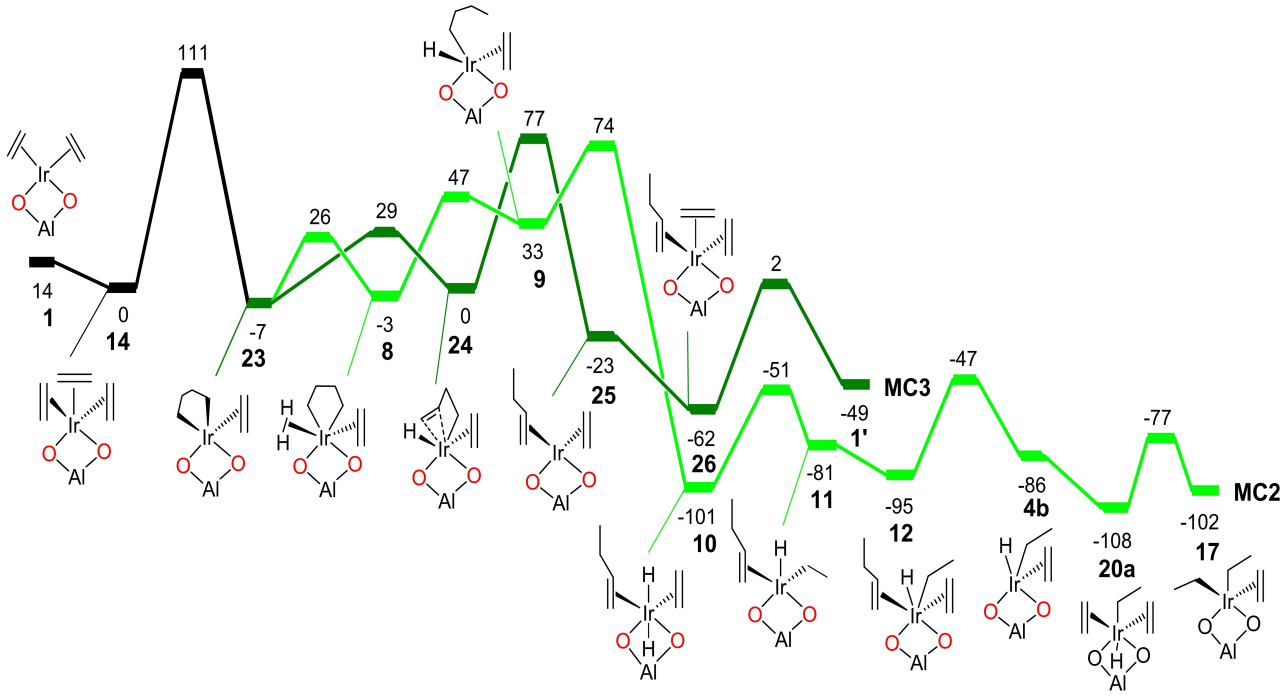

Figure 3. Simplified free energy profile for ethene dimerization via the pathways **MC2** and **MC3** at a 3-ligand Ir(I) complex **14**, $[Ir(C_2H_4)_3]^+$. Free energies (kJ mol^{-1}) with respect to complex **14** as well as H_2 and C_2H_4 in the gas phase, at infinite separation. Pathway **MC2** is shown in light green, pathway **MC3** in dark green. Other lay-out as in Figure 1. Although pathway **MC3** has a slightly higher crucial barrier, it is preferred by 46 kJ mol^{-1} over **MC2** when the energetic span is considered, δE(**MC3**) = 109 kJ mol^{-1} vs. δE(**MC2**) = 155 kJ mol^{-1}.

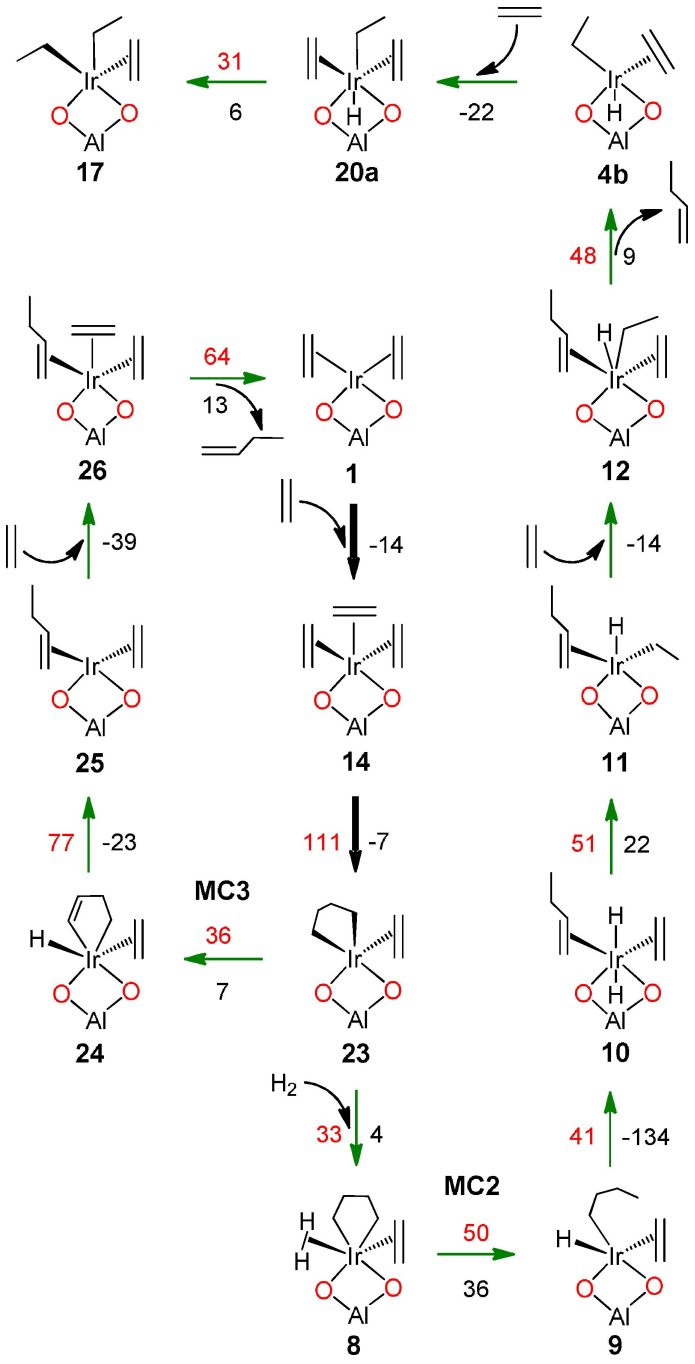

Scheme 4. Reaction network of ethene hydrogenation and dimerization using a 3-ligand model via the metallacycle pathways **MC2** and **MC3**. Lay-out as in Scheme 2. The starting complex **14** is formed along the route **17**→**16**→**15**→**14′**, Scheme 3.

An alternative route to the formation of ethane via **17**→**20b**→**21**→**22**→**1′** is discussed in Section S3 and Figure S3 of the Supporting Information.

C–C coupling variants. As a first route to the dimerization of ethene, we examined the direct C–C bond formation starting from complex **14**, $[Ir(C_2H_4)_3]^+$, via a metallacycle mechanism, which, in the 2-ligand case, was determined more favorable than the Cossee-Arlman mechanism. Starting from **14**, we studied the alternatives **MC2** and **MC3**, with the metallacyclopentane complex **23** as branching point between them, Scheme 4 and Figure 3.

Metallacycle mechanism MC2. The oxidative coupling of two ethene ligands in complex **14** is slightly exergonic, G_r(**14**→**23**) = −7 kJ mol^{-1}, leading to the metallacyclopentane species **23**. This step requires overcoming a substantial free energy barrier, G_a(**14**→**23**) = 111 kJ mol^{-1}, Scheme 4 and Figure 3. This barrier is by 30 kJ mol^{-1} higher than the competing crucial barrier for ethene hydrogenation, G_a(**14**→**15**) = 81 kJ mol^{-1},

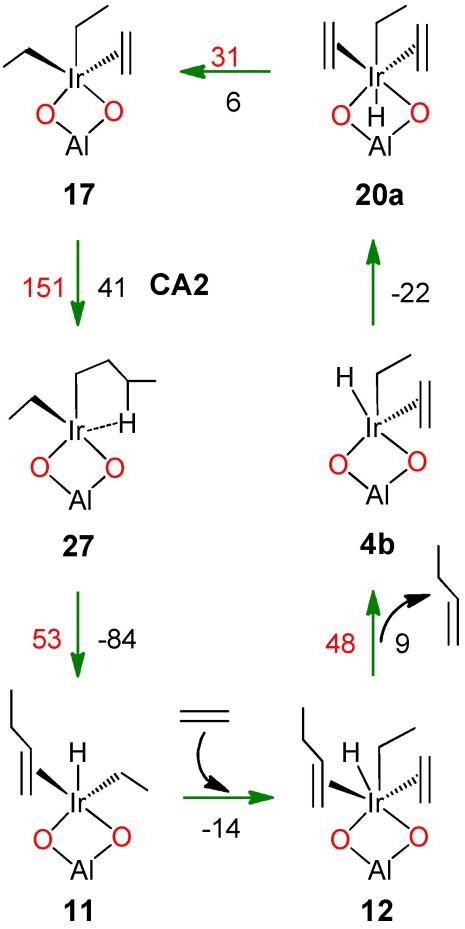

Scheme 5. Reaction network of ethene dimerization via a Cossee-Arlman mechanism, pathway **CA2**, using a 3-ligand model. Lay-out as in Scheme 2.

Scheme 3 and Figure 2, suggesting the formation of ethane to be preferred.

The coordination of hydrogen at the Ir center of the metallacyclopentane complex **23** is slightly endergonic, G_r(**23**→**8**) = 4 kJ mol^{-1}, leading back to complex **8**, over a moderate free energy barrier, G_a(**23**→**8**) = 33 kJ mol^{-1}, Scheme 4 and Figure 3. Therefore, complex **23** connects to the pathway **MC1** to form butene, with a subsequent product release via **8**→**9**→**10**→**11**→**12**→**4b**, Scheme 2. Finally, coordination of an additional ethene moiety to the Ir center of **4b** is exergonic, G_r(**4b**→**20a**) = −22 kJ mol^{-1}, forming complex **20a**, Scheme 4 and Figure 3. Note that complexes **20** and **20a** appear on their pathways after producing and releasing ethane or butene, respectively, Figures 2 and 3. This leads to a difference of 42 kJ mol^{-1} (−150 vs. −108 kJ mol^{-1} relative to **14**) between these complexes which corresponds to the difference in the calculated free energy of the products formed, 42 kJ mol^{-1}; ethane, −106 kJ mol^{-1} vs. butene, −64 kJ mol^{-1}, Figures 2 and 3. Complex **4b** connects to the crucial diethyl complex **17** via **4b**→**20a**→**17**, Scheme 4 and Figure 3. To note: complex **17** regenerates the initial complex **14** (as **14′**) via **17**→**16**→**15**→**14′**, thus closing the catalytic cycle, Scheme 3. Thus, the proposed pathway **MC2** produces one molecule of butene per catalytic cycle, Figure 3.

For Rh, we reported the pathway **MC2** to produce one molecule of ethane and butene per catalytic cycle.[5b] Revisiting the pathway **MC2** for Rh, with the present analogous pathway for Ir in mind, lead to a similar conclusion also in the case of Rh; for details, see Section S4, and Figure S4 of the Supporting Information.

Metallacycle mechanism MC3. The other variant for the dimerization from complex **23**, pathway **MC3**, Scheme 4, produces exclusively butene – without activation of molecular hydrogen. It starts with a β-hydrogen shift in complex **23**, from the metallacyclopentane ring to the Ir center, yielding the metal-hydride complex **24**, $[Ir(C_2H_4)(H)(C_4H_7)]^+$, G_r(**23**→**24**) = 7 kJ mol^{-1}, over a moderate free energy barrier, G_a(**23**→**24**) = 36 kJ mol^{-1}, Scheme 4 and Figure 3. Next, cleaving an Ir–CH_2 bond of the metallacycle ring in complex **24**, followed by an H transfer to that –CH_2 group leads to the butene complex **25**, $[Ir(C_2H_4)(C_4H_8)]^+$. This step is exergonic, G_r(**24**→**25**) = −23 kJ mol^{-1}, over a notable activation free energy barrier, G_a(**24**→**25**) = 77 kJ mol^{-1} (or an overall barrier of 84 kJ mol^{-1} above **23**), Scheme 4 and Figure 3. Subsequently, a further ethene moiety coordinates to the Ir center of **25** in exergonic fashion, G_r(**25**→**26**) = −39 kJ mol^{-1}, leading to complex **26**, $[Ir(C_2H_4)_2(C_4H_8)]^+$, Scheme 4 and Figure 3. As a final, slightly endergonic step, complex **26** regenerates **1** (as **1′**) by removing butene, G_r(**26**→**1′**) = 13 kJ mol^{-1}, over a moderate free energy barrier, G_a(**26**→**1′**) = 64 kJ mol^{-1}, thus closing the catalytic cycle, Scheme 4 and Figure 3.

Although pathway **MC3** has a crucial barrier that is by 3 kJ mol^{-1} higher than the analogous barrier of pathway **MC2** (84−81 kJ mol^{-1} relative to **23**), its energetic span (δE)[14] is lower by 46 kJ mol^{-1} than that of **MC2** δE(**MC3**) = 109 kJ mol^{-1} *vs* δE(**MC2**) = 155 kJ mol^{-1}, Figure 3 and Figure S5 of the Supporting Information.

C–C coupling from complex 17 via a Cossee-Arlman mechanism, CA2. The rate-determining C–C coupling step between one of the ethyl ligands and the ethene moiety in **17** yields the butyl complex **27**, $[Ir(C_2H_5)(C_4H_9)]^+$, G_r(**17**→**27**) = 41 kJ mol^{-1}, over a rather high free energy barrier, G_a(**17**→**27**) = 151 kJ mol^{-1}, Scheme 5 and Figure 2. Note, however, this crucial barrier of the path **CA2**, 99 kJ mol^{-1} above **1**, is by only 2 kJ mol^{-1} higher than the analogous C–C coupling barrier of the mechanisms **MC2** and **MC3**, 97 kJ mol^{-1} above **1**, Scheme 4, suggesting that both dimerization variants compete in the case of Ir.

Next, the butyl group in **27** rotates around its C1–C2 bond, associated with a concerted β-hydrogen transfer to the Ir center, Scheme 5. That highly exergonic step, G_r(**27**→**11**) = −84 kJ mol^{-1}, leads back to the desired butene complex **11**, $[Ir(C_2H_5)(H)(C_4H_8)]^+$, over a moderate barrier, G_a(**27**→**11**) = 53 kJ mol^{-1}, Scheme 5 and Figure 2. Thus, pathway **CA2** interconnects to the pathway **MC2**, regenerating complex **17** (as **17′**) via **11**→**12**→**4b**→**20a**→**17′**, Schemes 4 and 5, and Figure 2 and 3. Inspired by this outcome for Ir, we searched for an analogous connection between the pathway **CA2** and **MC2** for Rh, Section S4, and Figure S4 of the Supporting Information.

Also for 3-ligand Ir models, we observed oxidation state +3 as the dominant one, Figures 2 and 3, analogous to the case of Rh.[5b] For instance, one notes four complexes only, **14**, **15**, **25**, and **26**, with oxidation state +1, in contrast to the remaining 15 complexes with Ir in oxidation state +3, Figures 2 and 3. Ir(III) chemistry is dominating for 3-ligand models as evident from oxidation state +3 of complex **17**, the crucial branching point to ethene hydrogenation and dimerization, and also of complex **23** on the dimerization pathways **MC2** and **MC3**, Figures 2 and 3.

Alternative routes to the formation of butyl via various C–C coupling steps, namely **18**→**31**, and **20**→**32**, are discussed in Section S5 and Scheme S1 of the Supporting Information.

2-ligand vs 3-ligand based pathways

We compare the calculated barriers of the crucial hydrogenation and dimerization steps of the pathways determined for the 2-ligand and the 3-ligand models. The highest absolute free energy barrier for ethene hydrogenation on the 3-ligand pathway, namely TS **14**→**15**, 67 kJ mol^{-1} above **1**, is higher by 16 kJ mol^{-1} than the crucial hydrogen activation barrier for the 2-ligand model, TS **2**→**3**, 51 kJ mol^{-1} above **1**; cf. Schemes 3 and 2 as well as Figures 2 and 1. However, similar to the Rh(I) complex,[5b] we argue also here that the higher stability of complex **14**, by 61 kJ mol^{-1} compared to complex **2**, adds a bias to the ethene hydrogenation variant based on the 3-ligand model, Schemes 2 and 3. As to the C–C coupling, the crucial barrier along the 3-ligand based mechanisms **MC2** and **MC3** via TS **14**→**23**, 97 kJ mol^{-1} above **1**, is by 18 kJ mol^{-1} lower in absolute terms than the crucial barrier on the 2-ligand based pathway **MC1** via TS **3**→**7**, 115 kJ mol^{-1} above **1**, Figures 1 and 2. Thus, for C–C coupling, the 3-ligand variant **MC2** is preferred when the crucial barriers are compared. At the end of the following sub-section, we will revisit this aspect from the perspective of the energetic span concept.[14]

In summary, starting from complex **14**, the crucial barrier for ethene hydrogenation, G_a(**14**→**15**) = 81 kJ mol^{-1}, is by 30 kJ mol^{-1} lower in energy than the competing C − C coupling barrier, G_a(**14**→**23**) = 111 kJ mol^{-1}, Schemes 3 and 4. Thus, with our model results, one is able to rationalize the experimentally preferred formation of ethane, but not the rather low selectivity for butene in the experiment.[9] The experimentally observed selectivities, ethane (89%) and butene (11%), translate to a difference in the crucial barriers, relative to **14** as just discussed, of only ~5 kJ mol^{-1}.[15] Thus, lowering the C − C coupling barrier by ~25 kJ mol^{-1} (i.e., G_a(**14**→**23**) = 86 kJ mol^{-1}) would rationalize the experimental formation of butene.

Thus far, we discussed the preference of the 2- and 3-ligand based pathways mainly by arguing that the third ethene ligand, leading to **14**, binds by 61 kJ mol^{-1} (47 + 14 kJ mol^{-1}) more favorably at $[Ir(C_2H_4)_2]^+$ than the H_2 molecule, forming **2**, necessary for any conversion and thus, determining the starting complex $[Ir(C_2H_4)_3]^+$, **14**. For a more detailed assessment, one has to consider that the third ligand may also dissociate from the metal center. As additional aspect, note that the initial barrier towards the crucial complexes is only relevant for reaching the catalytic cycle, but not for any subsequent turnover, Scheme 6.

Therefore, we take this opportunity and shortly highlight the competition between the mechanisms through the energetic span[14] δE of each catalytic cycle by evaluating the TOF-determining intermediate, TDI, TOF-determining transition state, TDTS, and the reaction free energy of the corresponding cycle, ΔG_r. The latter value needs to be added to the energetic span when the TDI appears after the TDTS in the catalytic cycle. Recall that the energetic span is a criterion for assessing the reaction rate of a catalytic cycle.[14] From Scheme 7 and Figure S5 of the Supporting Information, one concludes that hydrogenation is actually preferred via the 2-ligand route with δE = 49 kJ mol^{-1} (TDTS[**5**→**6**] = 27 kJ mol^{-1}, TDI[**4**] = −22 kJ mol^{-1}) vs. 71 kJ mol^{-1} (TDTS[**18**→**19**] = 27 kJ mol^{-1}, TDI [**20**] = −150 kJ mol^{-1}, ΔG_r = −106 kJ mol^{-1}) for the 3-ligand pathway. On the other hand, for C–C coupling we discussed

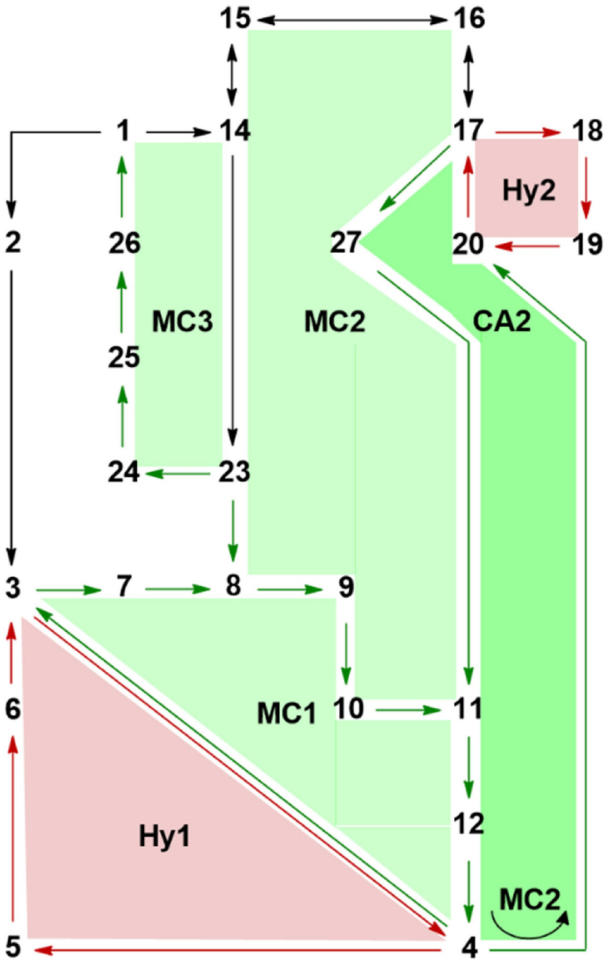

Scheme 6. Topology of the reaction network studied for ethene hydrogenation (**Hy**) – red – and dimerization – green – via Cossee-Arlman (**CA**) and metallacycle (**MC**) mechanisms for the zeolite-supported Ir(I)-diethene complex, $[Ir(C_2H_4)_2]^+$. Black arrows mark the common steps leading to the branching points, complexes **3** and **17**, for the pathways to ethane and 1-butene, and intermediate **23**, interconnecting the pathways **MC2** and **MC3**. Double-headed arrows indicate steps that may be passed in either direction.

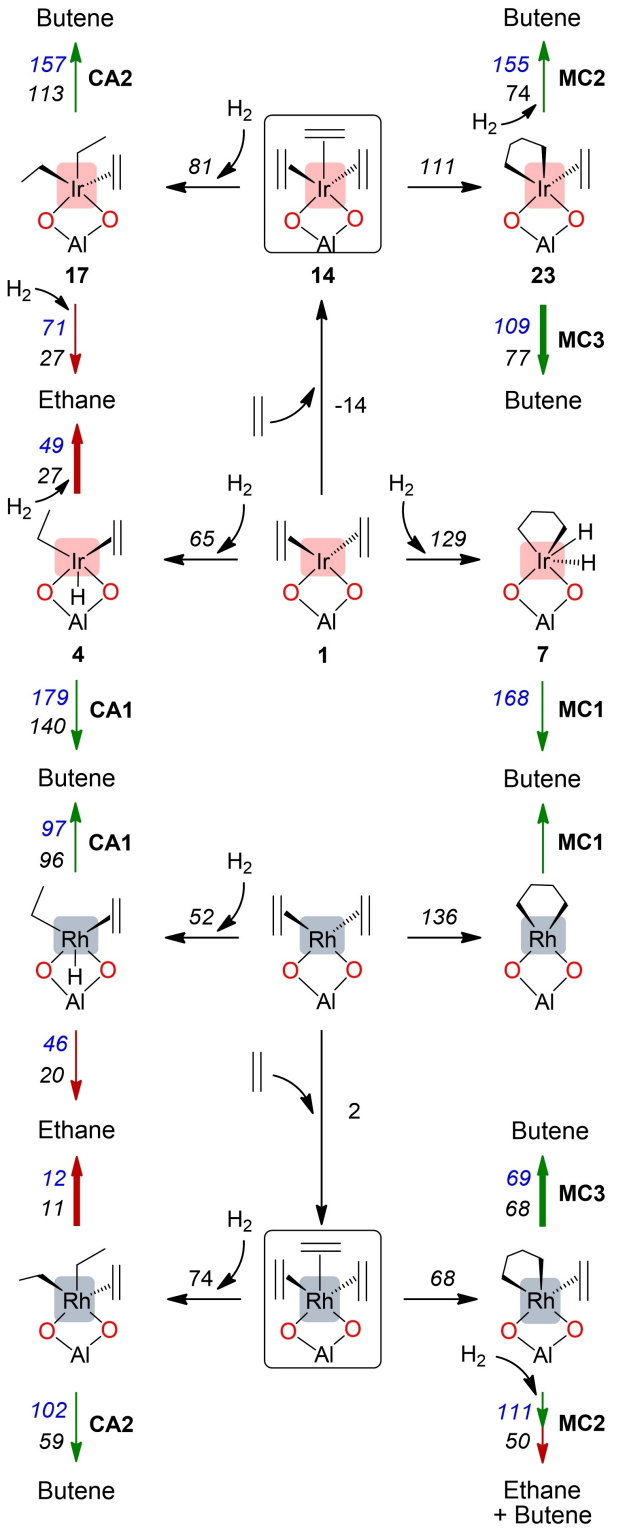

Scheme 7. Overview over the 2-ligand and 3-ligand based pathways studied for ethene hydrogenation and dimerization (the latter via Cossee-Arlman, **CA**, and metallacycle, **MC**, mechanisms) for the zeolite-supported M(I) diethene complexes, **1** $[M(C_2H_4)_2]^+$, M=Ir or Rh. Only crucial intermediates are shown. Absolute activation free energies (in kJ mol^{-1}) relative to the pertinent 3-ligand M(I) complex, $[M(C_2H_4)_3]^+$. Values δE of the energetic span are given in blue and italics. Bold arrows indicate the most favorable pathways according to the energetic span. Other layout choices as in Scheme 2.

already **MC3** as favored with $\delta E = 109$ kJ mol^{-1} (TDTS[**14**→**23**] = 111 kJ mol^{-1}, TDI[**26**] = −62 kJ mol^{-1}, $\Delta G_r = -64$ kJ mol^{-1}), while the values δE of the alternative pathways, **MC1**, **MC2**, and **CA2**, fall in the range of 155–168 kJ mol^{-1}, Scheme 7 and Figure S5 of the Supporting Information.

The experimental study showed[9] that a metal center on average supports 1–2 turnovers only. Thus, both initial turnover and energetic span may both contribute with about similar weights when estimating an overall preference of the studied 2- and 3-ligand pathways. Hence, when judging the pathways, one has to consider both, the start-up phase as well as the catalytic cycle.

The reaction network, Scheme 6, clearly shows that the various pathways of 2- and 3-ligand models are notably interconnected. This observation holds in particular for the intermediates **8** to **11** on the **MC1** cycle which also occur in the catalytic cycles of the mechanisms **MC2** and **CA2**. Furthermore, the 2-ligand hydrogenation cycle **Hy1** and the corresponding metallacycle mechanism **MC1** share the transformation **3**→**4** and its reverse **4**→**3**, Scheme 6. In fact, also each catalytic cycle of 3-ligand models, **Hy2**, **MC2**, **MC3**, and **CA2**, Scheme 6, share intermediates among each other and with the mechanisms of 3-ligand models. Intermediates **3**, **4**, and **17** entertain the most (four) direct connections, followed by intermediates **1**, **8**, **11**, **14**, **20**, and **23** with direct connections, Scheme 6.

Comparing analogous Ir vs Rh complexes for the ethene conversion mechanisms

Next we discuss how the choice of the metal M, M = Ir or Rh, affects the product selectivity, ethane *vs* butene, and the preferred ethene dimerization mechanism, Cossee-Arlman (**CA**) *vs* metallacycle (**MC**). To this end, we compare the results calculated for ethene conversion at the 3-ligand Ir(I) complex **14**, $[Ir(C_2H_4)_3]^+$, to the computational results previously obtained for the isostructural Rh(I) complex, $[Rh(C_2H_4)_3]^+$.[5b] As a side remark, we mention here a comparison of ethene conversion at 2-ligand M(I) complexes, $[M(C_2H_4)_2]^+$; M = Rh or Ir, see Section S6 of the Supporting Information.

Scheme 7 presents an overview over the 2- and 3-ligand based ethene hydrogenation and dimerization mechanisms, explored for the zeolite-supported M(I)-diethene starting complexes $[M(C_2H_4)_2]^+$; M = Ir or Rh. Hydrogenating the complex $[M(C_2H_4)_3]^+$ **14** forms the central di-ethyl moiety $[M(C_2H_4)(C_2H_5)_2]^+$ **17** which acts as a branching point between both transformation routes, ethene hydrogenation and dimerization, via a Cossee-Arlman mechanism, **CA2**, Scheme 7.

For Ir, the maximum free energy barrier on the path to forming ethane is higher by 7 kJ mol^{-1} (81–74 kJ mol^{-1}) than the analogous barrier for Rh. Similarly, the crucial barrier to butene formation is higher by 39 kJ mol^{-1} (113–74 kJ mol^{-1}) than the corresponding barrier of butene formation for Rh. Overall, for both Ir and Rh, the ethene hydrogenation barriers are lower than the barrier for the selective dimerization via pathway **CA2** by 86 kJ mol^{-1} (113–27 kJ mol^{-1}) and 48 kJ mol^{-1} (59–

11 kJ mol^{-1}), respectively. This suggests that ethane is formed as the major product, Scheme 7.

An alternative route to ethene dimerization proceeds *via* first forming metallacycle complexes, pathways **MC2** and **MC3**. For Ir, the crucial oxidative C–C coupling barrier is higher by 43 kJ mol^{-1} (111–68 kJ mol^{-1}) than the analogous barrier for Rh, Scheme 7 and Figure S4 of the Supporting Information. Importantly, the latter barrier for Ir via a **MC** mechanism, 111 kJ mol^{-1}, is lower by 2 kJ mol^{-1} than the analogous C–C coupling barrier for the **CA** mechanism, 113 kJ mol^{-1}, suggesting that both mechanisms compete in the case of Ir, Scheme 7. Thus, from these calculated results, one expects the formation of ethane only for the Ir(I) complex **1**, $[Ir(C_2H_4)_2]^+$, Schemes 3 and 4, and Figures 2 and 3. At variance, for Rh(I), the **MC** mechanism is more favorable than the **CA** mechanism, with absolute free energy barriers of 68 kJ mol^{-1} and 74 kJ mol^{-1}, respectively, Scheme 7. Therefore, for Rh, the previously reported pathway **MC2**,[5b] rationalizes the experimental formation of both ethane and butene, Scheme 7.

Overall, these results suggest that substituting Rh by Ir significantly increases the crucial oxidative C–C coupling barrier by 43 kJ mol^{-1} (111–68 kJ mol^{-1}), thus severely hindering the **MC** mechanism for the Ir system.

To explore the calculated difference in the oxidative C–C coupling barrier heights, we analyzed the structures of the corresponding transition states, TS **14**→**23**, where **M** = Ir or Rh, Figure 4. The crucial distances in the structure of TS **14**→**23**, M=Ir, Ir–C1=238 pm and Ir–C2 = 232 pm, are significantly shorter by 29 pm and 20 pm, respectively, than the corresponding distances in the analogous TS structure for the Rh(I) complex, **14**→**23**, M = Rh, Rh–C1 = 267 pm and Rh–C2 = 252 pm, Figure 4. Concomitantly, the C–C distance of the C1–C2 bond to be formed is 15 pm longer for Ir than for Rh, C–C = 210 pm vs C–C = 195 pm, respectively. Additionally, the distances Ir–O = 235–241 pm are somewhat more symmetric compared to the analogous distances Rh–O = 225–240 pm, Figure 4.

Overall, these results suggest that the stability of the TS structure is inversely related to the C–C distance: the longer the C1–C2 distance in the TS, the higher lies the TS structure. In consequence, the studied oxidative C–C coupling reaction is much easier in the case of Rh than of Ir. To understand the reason why crucial M–C1 and M–C2 bond lengths are shorter for Ir when compared to Rh, we carried out constrained optimizations starting from complex **14**, by setting a series of specific values of four M–C distances to two ethene moieties, one equatorial and one axial, Figure S7 of Supporting Information. These additional results show that in the Ir system, one encounters a substantially higher energy penalty, by 30–50 kJ mol^{-1}, when M–C distances are elongated. Thus, for Ir, the TS structure of **14**→**23** for butene formation exhibits shorter M–C distances, which in turn induces a longer C1–C2 distance of the carbon-carbon bond to be formed. Overall, these geometrical differences lead to a higher activation barrier in the case of Ir compared to Rh and ultimately to a change in selectivity, disfavoring butene formation in the Ir complex.

Now we turn to the energetic span model for Rh which confirms the trends discussed for Ir. Hydrogenation and C–C coupling via the pathway **MC3** both are preferred via the 3-ligand Rh model with δE = 12 kJ mol^{-1} (TDTS[**14**→**17**] = 74 kJ mol^{-1}, TDI[**17**] = −44 kJ mol^{-1}, ΔG_r = −106 kJ mol^{-1}) and 69 kJ mol^{-1} (TDTS[**4**→**23**] = 68 kJ mol^{-1}, TDI[**26**] = −65 kJ mol^{-1}, ΔG_r = −64 kJ mol^{-1}), respectively, Scheme 7 and Figure S6 of the Supporting Information. Alternative C–C coupling pathways for Rh have δE values in the range of 97–111 kJ mol^{-1}, indicating that the energetic span of C–C coupling is by 40–70 kJ mol^{-1} lower than in the case of Ir, Scheme 7. In this way, one is able to rationalize the observed product distributions.

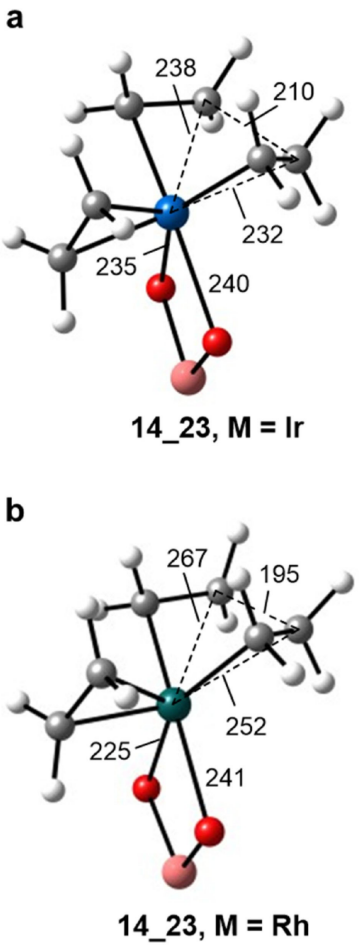

Figure 4. Comparison of crucial oxidative C–C coupling TS structures **14** **23** of ethene dimerization via the 3-ligand model based **MC** mechanism for the cases of (a) Ir and (b) Rh; see Scheme 4. Only the active complex is shown for clarity. Selected distances in pm. Color coding of the atoms: grey – carbon; white – hydrogen; red – oxygen; pink – aluminum; blue – iridium; teal – rhodium.

Conclusions

DFT calculations on QM/MM embedded cluster models were applied to study ethene conversion mechanisms at the zeolite-supported Ir(I) complex **1**, $[Ir(C_2H_4)_2]^+$. Starting from the 3-ligand complex $[Ir(C_2H_4)_3]^+$, we determined that the crucial diethyl intermediate $[Ir(C_2H_4)(C_2H_5)_2]^+$ yields exclusively ethane rather

than butene, which is most facile *via* a metallacycle mechanism. Finally, a comparison of the preferred 3-ligand model based ethene conversion mechanisms revealed that substituting Rh by Ir causes a switch in selectivity to exclusive ethene hydrogenation due to significantly increased C–C coupling barriers, by ~30 kJ mol^{-1} relative to Rh.

Overall, the detailed ethene conversion mechanisms elucidated here for the zeolite-supported complex $[Ir(C_2H_4)_2]^+$ differ to some extent from the experimental results as the models explored predict the formation of ethane only. In other words, we were unable to trace the 11% butene selectivity reported in experiments on Ir(I) complexes. Other effects may contribute to these experimental findings, e.g., some C–C coupling reactivity of the zeolite itself as reported for higher temperatures.[16] Irrespective of such effects, not discussed in the present work, note that the experimentally observed selectivities, ethane (89%) and butene (11%), translate to a difference in crucial (absolute) barriers of only ~5 kJ mol^{-1},[15] which at present is below the typical accuracy of economic DFT methods for systems of the complexity discussed here.[17] Nevertheless, the current DFT based QM/MM study allowed us to develop an extended picture of the catalytic hydrogenation and dimerization of ethene on single-site supported Ir(I) catalyst. Also, we were able to offer sufficient insight into how the nature of the metal affects the studied catalytic processes, ranging from switch in product selectivity to preferred pathway for the dimerization.

From a conceptual point of view as well as with regard to computational modeling, it seems appropriate to discriminate two classes of single-site catalysts: (*i*) single (transition) metal atoms on a metal or metal oxide support, and (*ii*) mononuclear (transition) metal complexes on inorganic porous supports like zeolites and metal oxides. Such single-site catalysts have recently intensively been discussed as bridging related heterogeneous and homogeneous catalytic processes.[18] Similar to the single metal atoms on a metal oxide support, the faujasite supported Ir(I) species discussed here also offers single active transition metal atoms, allowing one to determine the nature of active sites and the reaction mechanism *via* computational modelling. Both types of single-site catalysts reach the limit of maximum atom efficiency.[19] Note that faujasite supported Ir(I) species by themselves act as catalyst, while ethene serves as both ligand and reactant. However, as demonstrated by the present work, single atom catalysis may not necessarily be simpler (less complex) than catalysis on metal surfaces. The complexity is due to a plethora of ligand configurations and orientations. A second aspect is the interplay between the flexibility of multiple adsorption complexes and their conversions that renders modelling such systems challenging. We were able to highlight the complexity of the system by elaborating the connection between the catalytic cycles producing ethane or butene.

Computational Methods

We modeled faujasite (FAU) used in the experiments[6] as support of the various transition metal complexes. Faujasite is a zeolite with a highly symmetric cubic structure that belongs to space group $Fd\bar{3}m$. The structure features only a single, crystallographically distinct tetrahedral (T) site, surrounded by four symmetry-distinct oxygen centers, O1 to O4, Figure S1 of the Supporting Information.[20] Similar to the Rh(I) system, we modeled the Ir(I) complex **1**, $[Ir(C_2H_4)_2]^+$ by anchoring the metal center at the sites O1 and O4 on the twelve-member ring (12-MR) of the supercage. The analogous arrangement had been determined most stable for Rh,[21] Figure S1 of the Supporting Information.

In the same spirit, we used an 83T cluster,[22] taken from the zeolite lattice, to model the ethene conversion activity at a Ir(I) center anchored in FAU. This cluster model comprises a supercage unit with additional sodalite cages and hexagonal prisms, with 278 atoms in total, Figure S1a of the Supporting Information. The surface oxygen centers are located at least 400 pm away from the Ir center. Within this 83T cluster, we used a QM partition of 5T centers which contains the AlO_4 moiety carrying the metal complex, surrounded by 4 neighboring Si units, Figure S1b of the Supporting Information. This hybrid QM/MM 5/83T model was treated with the ONIOM approach,[23] a strategy which was reported[22] to be equally well-suited as periodic models for describing the catalytic reactions addressed in the present study.

All electronic structure calculations were carried out with the Gaussian 09 program suite.[24] The high-level partition of the ONIOM calculations (5T) was treated using the PBE exchange-correlation functional[25] and with split-valence 6–31G(d,p) basis sets[26] for H, C, O, Al, and Si. For Ir, we used the quasirelativistic Stuttgart/Dresden effective core potential MWB28 with the associated valence basis set (standard SDD keyword in Gaussian 09).[27] The remainder of the 83T atoms was assigned as low-level (MM) partition, surrounding the QM zeolite partition, and treated with the universal force field (UFF).[28] This combined theoretical method ONIOM(PBE:UFF) was applied to the considered 5/83T embedded cluster model.[22] The geometry optimizations were carried out without symmetry constraints.

We characterized resulting stationary points, representing either local minima or transition state structures, using a harmonic normal mode analysis, at the same level of theory as the corresponding geometry optimization. For a better energetics, energies of all stationary configurations were re-evaluated via single-point calculations using the more flexible basis sets 6–311++G(2d,p)[26] for H, C, O, Al, and Si. Similar to our previous work, the reported gas phase free energies were obtained here from the electronic energies estimated at the PBE/6-311++G(2d,p) level, corrected with zero-point energies and thermal corrections evaluated with harmonic frequencies calculated at the PBE/6-31G(d,p) level at standard conditions, 298 K and 1 atm. We reference reactants and products to their free energies in the gas phase. Note that transferring these species to a zeolite cavity would introduce changes of -5 kJ mol^{-1} to 4 kJ mol^{-1} for hydrocarbons and 15 kJ mol^{-1} for H_2.[5a] However, as most of these effects are small in comparison to the activation energies, we refrained from discussing these extra steps in the pertinent processes, in particular to keep the computational approach as in our previous work on Rh(I) complexes.[5]

We labeled each intermediate by a unique number. In the free energy profiles, we add a prime to these labels should an intermediate be produced again on a given reaction path when closing a catalytic cycle; this second intermediate features a different energy as a product has been formed on the way.

Similarly, when the same intermediate appears again, we augment the numerical labels by letters a, b, c, etc. When discussing reaction steps, we reference the reaction energy relative to the first intermediate mentioned, e.g., for the sequence **x**→**y**→**z** we quote the energy of the reaction leading to **z** with respect to **x**. We usually mention the heights of relative free energy barriers with respect to the immediately preceding intermediate, unless stated otherwise.

Acknowledgments

*This work was supported by grant no.1527700033 from the A*STAR Science and Engineering Research Council as well as generous allotments of computational resources at the A*STAR Computational Resource Centre (ACRC) and the National Supercomputing Centre Singapore. S.V. acknowledges the support from A*STAR AME IAF-PP grant (Grant No. A19E9a0103).*

Conflict of Interest

The authors declare no conflict of interest.

Keywords: Zeolite-supported Ir(I) · C–C coupling · Ethene hydrogenation · Density functional calculations · QM/MM model

[1] a) L. Liu, A. Corma, *Chem. Rev.* **2018**, *118*, 4981–5079; b) Z. Li, S. Ji, Y. Liu, X. Cao, S. Tian, Y. Chen, Z. Niu, Y. Li, *Chem. Rev.* **2020**, *120*, 623–682.
[2] a) M. Flytzani-Stephanopoulos, B. C. Gates, *Annu. Rev. Chem. Biomol. Eng.* **2012**, *3*, 545–574; b) X.-F. Yang, A. Wang, B. Qiao, J. Li, J. Liu, T. Zhang, *Acc. Chem. Res.* **2013**, *46*, 1740–1748; c) J. Liu, *ACS Catal.* **2017**, *7*, 34–59; d) B. C. Gates, M. Flytzani-Stephanopoulos, D. A. Dixon, A. Katz, *Catal. Sci. Technol.* **2017**, *7*, 4259–4275; e) S. Pellizzeri, M. Barona, V. Bernales, P. Miró, P. Liao, L. Gagliardi, R. Q. Snurr, R. B. Getman, *Catal. Today*. **2018**, *312*, 149–157; f) P. Christopher, *ACS Energy Lett.* **2019**, *4*, 2249–2250.
[3] E. Groppo, G. A. Martino, A. Piovano, C. Barzan, *ACS Catal.* **2018**, *8*, 10846–10863.
[4] B. Chowdhury, J. J. Bravo-Suárez, N. Mimura, Lu, K. K. Bando, S. Tsubota, M. Haruta, *J. Phys. Chem. B* **2006**, *110*, 22995–22999.
[5] a) S. V. C. Vummaleti, A. Genest, N. Kuriakose, N. Rösch, *ACS Catal.* **2018**, *8*, 9836–9846; b) S. V. C. Vummaleti, N. Kuriakose, S. Dinda, Y. Wu, A. Genest, N. Rösch, *Catal. Sci. Technol.* **2019**, *9*, 2781–2793.
[6] a) P. Serna, B. C. Gates, *J. Am. Chem. Soc.* **2011**, *133*, 4714–4717; b) P. Serna, B. C. Gates, *Angew. Chem. Int. Ed.* **2011**, *50*, 5528–5531; *Angew. Chem.* **2011**, *123*, 5642–5645.
[7] a) P. Cossee, *Tetrahedron Lett.* **1960**, *1*, 12–16; b) P. Cossee, *J. Catal.* **1964**, *3*, 80–88; c) E. J. Arlman, P. Cossee, *J. Catal.* **1964**, *3*, 99–104.
[8] R. Robinson, D. S. McGuinness, B. F. Yates, *ACS Catal.* **2013**, *3*, 3006–3015.
[9] a) J. Lu, C. Martinez-Macias, C. Aydin, N. D. Browning, B. C. Gates, *Catal. Sci. Technol.* **2013**, *3*, 2199–2203; b) C. Martinez-Macias, P. Serna, B. C. Gates, *ACS Catal.* **2015**, *5*, 5647–5656.
[10] M. R. Momeni, D. R. Pahls, D. Yang, T. C. Wang, O. K. Farha, J. T. Hupp, C. J. Cramer, L. Gagliardi, B. C. Gates, *J. Am. Chem. Soc.* **2017**, *139*, 18406–18406.
[11] M. R. Momeni, D. R. Pahls, D. Yang, S. O. Odoh, J. Borycz, T. C. Wang, O. K. Farha, J. T. Hupp, C. J. Cramer, L. Gagliardi, B. C. Gates, *ACS Catal.* **2018**, *8*, 2364–2364.
[12] D. Yang, M. R. Momeni, H. Demir, D. R. Pahls, M. Rimoldi, T. C. Wang, O. K. Farha, J. T. Hupp, C. J. Cramer, B. C. Gates, L. Gagliardi, *Faraday Discuss.* **2017**, *201*, 195–206.
[13] For standard Gibbs free energy values of formation of 1-butene and ethane: J. A. Dean. Lange's Hand Book of Chemistry, *Ed.* 15 (Eds.: J. A. Dean), McGraw-Hill, New York, **1992**, pp. 6.10-6.24.
[14] S. Kozuch, S. Shaik, *Acc. Chem. Res.* **2011**, *44*, 101–110.
[15] K. J. Laidler, M. C. King, *J. Phys. Chem.* **1983**, *87*, 2657–2664.
[16] a) S. Namuangruk, P. Pantu, J. Limtrakul, *ChemPhysChem* **2005**, *6*, 1333–1339; b) W. Shen, *Micropor Mesopot Mat.* **2017**, *247*, 136–144.
[17] Y. Sun, L. Hu, H. Chen, *J. Chem. Theory Comput.* **2015**, *11*, 1428–1438.
[18] A. Wang, J. Li, T. Zhang, *Nat. Chem. Rev.* **2018**, *2*, 65–81.
[19] L. Li, X. Chang, X. Lin, Z.-J. Zhao, J. Gong, *Chem. Soc. Rev.* **2020**, *49*, 8156–8178.
[20] D. Olson, E. Dempsey, *J. Catal.* **1969**, *13*, 221–231.
[21] A. Govindasamy, V. K. Markova, A. Genest, N. Rösch, *Catal. Sci. Technol.* **2017**, *7*, 102–113.
[22] S. Dinda, A. Govindasamy, A. Genest, N. Rösch, *J. Phys. Chem. C* **2014**, *118*, 25077–25088.
[23] M. Svensson, S. Humbel, R. D. Froese, T. Matsubara, S. Sieber, K. Morokuma, *J. Phys. Chem.* **1996**, *100*, 19357–19363.
[24] M. J. Frisch, G. W. Trucks, H. B. Schlegel, G. E. Scuseria, M. A. Robb, J. R. Cheeseman, G. Scalmani, V. Barone, B. Mennucci, G. A. Petersson, H. Nakatsuji, M. Caricato, X. Li, H. P. Hratchian, A. F. Izmaylov, J. Bloino, G. Zheng, J. L. Sonnenberg, M. Hada, M. Ehara, K. Toyota, R. Fukuda, J. Hasegawa, M. Ishida, T. Nakajima, Y. Honda, O. Kitao, H. Nakai, T. Vreven, J. J. A. Montgomery, J. E. Peralta, F. Ogliaro, M. Bearpark, J. J. Heyd, E. Brothers, K. N. Kudin, V. N. Staroverov, R. Kobayashi, J. Normand, K. Raghavachari, A. Rendell, J. C. Burant, S. S. Iyengar, J. Tomasi, M. Cossi, N. Rega, J. M. Millam, M. Klene, J. E. Knox, J. B. Cross, V. Bakken, C. Adamo, J. Jaramillo, R. Gomperts, R. E. Stratmann, O. Yazyev, A. J. Austin, R. Cammi, C. Pomelli, J. W. Ochterski, R. L. Martin, K. Morokuma, V. G. Zakrzewski, G. A. Voth, P. Salvador, J. J. Dannenberg, S. Dapprich, A. D. Daniels, Ö. Farkas, J. B. Foresman, J. V. Ortiz, J. Cioslowski, D. J. Fox, Gaussian 09, Revision A.2, Gaussian, Inc. Wallingford, CT, **2009**.
[25] J. P. Perdew, K. Burke, M. Ernzerhof, *Phys. Rev. Lett.* **1996**, *77*, 3865–3868.
[26] J. S. Binkley, J. A. Pople, W. J. Hehre, *J. Am. Chem. Soc.* **1980**, *102*, 939–947.
[27] D. Andrae, U. Häußermann, M. Dolg, H. Stoll, H. Preuß, *Theor. Chim. Acta.* **1990**, *77*, 123–141.
[28] A. K. Rappé, C. J. Casewit, K. S. Colwell, W. A. Goddard III, W. M. Skiff, *J. Am. Chem. Soc.* **1992**, *114*, 10024–10035.

Manuscript received: April 27, 2021
Revised manuscript received: May 21, 2021
Version of record online: June 17, 2021